2-28-2003

# Near-field calculations for a rigid spheroid with an arbitrary incident acoustic field

John P. Barton
*University of Nebraska - Lincoln*

Nicholas L. Wolff
*University of Nebraska - Lincoln*

Haifeng Zhang
*University of Nebraska - Lincoln*

Constantine Tarawneh
*The University of Texas Rio Grande Valley*, constantine.tarawneh@utrgv.edu



## Recommended Citation

Barton, J. P., Wolff, N. L., Zhang, H., & Tarawneh, C. (2003). Near-field calculations for a rigid spheroid with an arbitrary incident acoustic field. The Journal of the Acoustical Society of America, 113(3), 1216–1222. https://doi.org/10.1121/1.1538200

# Near-field calculations for a rigid spheroid with an arbitrary incident acoustic field

John P. Barton,[a] Nicholas L. Wolff, Haifeng Zhang, and Constantine Tarawneh
*Department of Mechanical Engineering, College of Engineering & Technology, University of Nebraska—Lincoln, Lincoln, Nebraska 68588-0656*

(Received 15 February 2002; revised 8 November 2002; accepted 25 November 2002)

A general spheroidal coordinate separation-of-variables solution is developed for the determination of the acoustic pressure distribution near the surface of a rigid spheroid for a monofrequency incident acoustic field of arbitrary character. Calculations are presented, for both the prolate and oblate geometries, demonstrating the effects of incident field orientation and character (plane-wave, spherical wave, cylindrical wave, and focused beam) on the resultant acoustic pressure distribution.
 [DOI: 10.1121/1.1538200]

PACS numbers: 43.20.El, 43.20.Fn, 43.20.Bi, 43.35.Ae [LLT]

## I. INTRODUCTION

The theoretical determination of the acoustic scattering that results from the interaction of an incident plane wave or point source with a rigid, fixed-position prolate spheroid has been previously considered. The problem has been addressed using the spheroidal coordinate separation-of-variables approach,[1–9] using the spherical coordinate extended boundary method (sometimes equivalently referred to as the T-matrix method),[10–12] and, recently, using a cylindrical function deformed cylinder method.[13] The rigid oblate spheroid scattering problem has apparently drawn less interest.[14] These earlier works were predominantly concerned with farfield scattering or, at most, the determination of the acoustic pressure at the surface of the spheroid. In addition, many of these earlier works are not general solutions, but are restricted in some way, requiring end-on incidence or a high-frequency/high aspect ratio asymptotic limit.

The study presented here, a spheroidal coordinate separation-of-variables solution of the rigid spheroid acoustic scattering problem, differs from earlier efforts in that (1) the incident field can be any known monofrequency field (e.g., a focused acoustic beam or the scattered field from an adjacent object), not just a plane wave or a point source and (2) the solution for the oblate spheroid, as well as the prolate spheroid, is included.

## II. THEORETICAL DEVELOPMENT

The interaction of a known incident monofrequency acoustic field with a motionless, rigid spheroid is considered. The medium surrounding the spheroid is assumed to be homogeneous, infinite, and nonabsorbing. A schematic of the geometrical arrangement is given in Fig. 1. An implicit time dependence of $\exp(-i\omega t)$ is assumed and the acoustic pressure is nondimensionalized relative to a reference acoustic pressure amplitude associated with the incident field ($p_r$).

A spheroidal surface can be created by rotating an ellipse about its axis. If the ellipse is rotated about its major axis, a prolate spheroid is formed. If the ellipse is rotated about its minor axis, an oblate spheroid is formed. If $a$ is the length of the semimajor axis and $b$ is the length of the semiminor axis, then

$$f=a[1-(b/a)^2]^{1/2}, \tag{1}$$

where $f$ is the semifocal length of the spheroid. In the following, the rectangular coordinates $(x,y,z)$, the spatial position vector $\mathbf{r}$, and the vector calculus operators $(\nabla,\nabla^2)$ are all nondimensionalized relative to the semifocal length $f$.

In prolate coordinates, the normalized rectangular coordinates are related to the spheroidal coordinates $(-1<\eta<+1, 1<\xi<\infty, 0<\phi<2\pi)$ by

$$x=[(\xi^2-1)(1-\eta^2)]^{1/2}\cos\phi, \tag{2}$$

$$y=[(\xi^2-1)(1-\eta^2)]^{1/2}\sin\phi, \tag{3}$$

$$z=\xi\eta, \tag{4}$$

where $\xi$ is the spheroidal radial coordinate, $\eta$ is the spheroidal angle coordinate, and $\phi$ is the azimuthal angle. A surface of constant $\xi=\xi_0$ forms the surface of a prolate spheroid with an axis ratio of

$$(a/b)=\frac{\xi_0}{(\xi_0^2-1)^{1/2}}. \tag{5}$$

So, for example, if $\xi_0=1.15470$ then $(a/b)=2$, if $\xi_0=1.060\,66$ then $(a/b)=3$, etc.

In oblate coordinates, the normalized rectangular coordinates are related to the spheroidal coordinates $(-1<\eta<+1, 0<\xi<\infty, 0<\phi<2\pi)$ by

$$x=[(\xi^2+1)(1-\eta^2)]^{1/2}\cos\phi, \tag{6}$$

$$y=[(\xi^2+1)(1-\eta^2)]^{1/2}\sin\phi, \tag{7}$$

$$z=\xi\eta. \tag{8}$$

In this case, a surface of constant $\xi=\xi_0$ forms the surface of an oblate spheroid with an axis ratio of

$$(a/b)=[1+(1/\xi_0^2)]^{1/2}. \tag{9}$$

So, for example, if $\xi_0=0.577\,35$ then $(a/b)=2$, if $\xi_0=0.353\,55$, then $(a/b)=3$, etc.

[a]Electronic mail: jbarton@unlserve.unl.edu

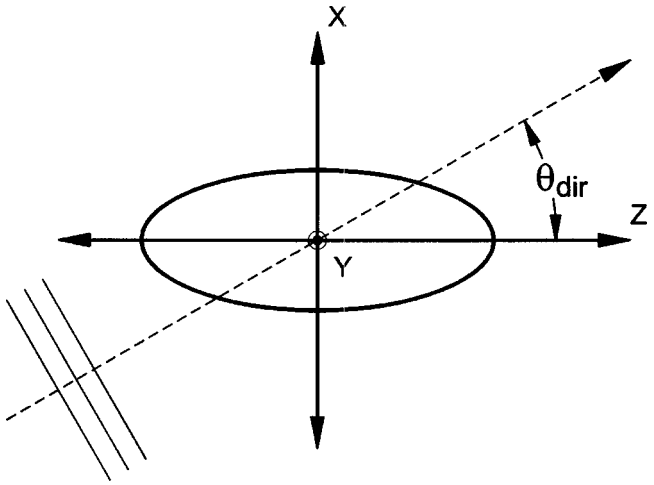


FIG. 1. Schematic of the geometrical arrangement. The spheroid is axisymmetric about the $z$ axis. For the prolate spheroid (as shown) the major axis is along the $z$ axis. For an oblate spheroid, the major axis would be perpendicular to the $z$ axis.

The eigenfunctions of the spheroidal coordinate separation-of-variables solution of the time-independent wave equation (Helmholtz equation),

$$\nabla^2 p + h^2 p = 0, \tag{10}$$

are of the form

$$p_{lm} = S_{lm}(h,\eta) R_{lm}^{(j)}(h,\xi) e^{im\phi}, \tag{11}$$

where $h = kf = 2\pi f/\lambda$ is the spheroidal size parameter, $S_{lm}$ is the spheroidal angle function, $R_{lm}^{(j)}$ is the spheroidal radial function [which may be of the first kind, $R_{lm}^{(1)}$, second kind, $R_{lm}^{(2)}$, third kind, $R_{lm}^{(3)} = R_{lm}^{(1)} + iR_{lm}^{(2)}$, or fourth kind, $R_{lm}^{(4)} = R_{lm}^{(1)} - iR_{lm}^{(2)}$], and the azimuthal dependence is contained in the complex exponential, $\exp(im\phi)$. The $S_{lm}$ and $R_{lm}^{(j)}$ functions depend on $h$ and are different for the prolate and oblate coordinate systems. $l$ and $m$ are integer indexes with $-\infty < m < \infty$ and, for a given value of $m$, $|m| < l < \infty$. A computer program for generating the associated eigenvalues, $\lambda_{lm}(h)$, and subroutines for generating the $S_{lm}$ and $R_{lm}^{(j)}$ functions were written based on the procedures described in Flammer.[15,16] (See also, for example, Refs. 17–21.)

The incident acoustic pressure (assumed known) can be expressed in terms of a general eigenfunction expansion of the form

$$p^{(i)}(\xi,\eta,\phi) = \sum_{l,m} A_{lm} S_{lm}(h,\eta) R_{lm}^{(1)}(h,\xi) e^{im\phi}, \tag{12}$$

and the appropriate form of the eigenfunction expansion for the resultant scattered acoustic pressure (to be determined) is given by

$$p^{(s)}(\xi,\eta,\phi) = \sum_{l,m} a_{lm} S_{lm}(h,\eta) R_{lm}^{(3)}(h,\xi) e^{im\phi}. \tag{13}$$

In Eq. (12), only $R_{lm}^{(1)}$ is included in the expansion for the incident field since $R_{lm}^{(2)}$ becomes unbounded as $\xi$ approaches the coordinate origin. In Eq. (13), $R_{lm}^{(3)}$ is used in the expansion for the scattered field since in the limit of large $\xi$ this function corresponds to an outgoing traveling wave, appropriate for the scattered field solution. (In this same limit, the $R_{lm}^{(4)}$ function would correspond to an incoming traveling wave.) In practice, the double summation indexes are truncated such that $-M < m < M$ and $|m| < l < L$, where $M$ and $L$ are chosen sufficiently large for convergence of the solution.

The expansion coefficients for the incident field, $A_{lm}$, can be determined by evaluating the series expression for the incident field, as given in Eq. (12), at the surface of the spheroid, $\xi = \xi_0$, and then applying the orthogonality condition of the angle functions,

$$\int_0^{2\pi} \int_{-1}^{1} [S_{lm}(h,\eta) e^{im\phi}][S_{l'm'}(h,\eta) e^{-im'\phi}] d\eta\, d\phi = 2\pi N_{lm} \delta_{l,l'} \delta_{m,m'}; \tag{14}$$

thus

$$A_{lm} = \frac{1}{2\pi N_{lm} R_{lm}^{(1)}(h,\xi_0)} \int_0^{2\pi} \int_{-1}^{1} [p^{(i)}(\xi_0,\eta,\phi) \times S_{lm}(h,\eta) e^{-im\phi}] d\eta\, d\phi, \tag{15}$$

where $N_{lm}$ is a constant that can be determined from the associated spheroidal function parameters, $d_r^{lm}$ (see p. 22 of Flammer[15]),

$$N_{lm} = \int_{-1}^{1} [S_{lm}(h,\eta)]^2 d\eta = 2 \sum_{r=0',1'}^{\infty} \frac{(r+2m)!\,(d_r^{lm})^2}{(2r+2m+1)r!}, \tag{16}$$

where the summation is over even integers if $(l-m)$ is even and is over odd integers if $(l-m)$ is odd. The scattered field expansion coefficients, $a_{lm}$, can be directly related to the corresponding incident field coefficients, $A_{lm}$, by an application of the boundary condition that at the surface of the rigid spheroid the normal ($\xi$) component of the acoustic velocity must be zero. Since the acoustic velocity is directly proportional to the gradient of the acoustic pressure, and since the acoustic field consists of a sum of the incident and scattered fields, at $\xi = \xi_0$,

$$\frac{\partial p^{(s)}}{\partial \xi} + \frac{\partial p^{(i)}}{\partial \xi} = 0, \tag{17}$$

or, equivalently,

$$\frac{\partial p^{(s)}}{\partial \xi} = -\frac{\partial p^{(i)}}{\partial \xi}. \tag{18}$$

The series expansions for $p^{(s)}$ and $p^{(i)}$ are substituted into Eq. (18) and the series terms are equated mode-by-mode, which gives the following direct relationship between $a_{lm}$ and $A_{lm}$:

$$a_{lm} = -\frac{R_{lm}^{(1)\prime}(h,\xi_0)}{R_{lm}^{(3)\prime}(h,\xi_0)} A_{lm}. \tag{19}$$

In summary, the procedure for determining the near-field acoustic pressure distribution for a rigid spheroid with a known incident field is as follows. The expansion coefficients of the incident field, $A_{lm}$, are calculated by numerical integration using Eq. (15). The expansion coefficients for the scattered field, $a_{lm}$, are then directly calculated from the $A_{lm}$

values using Eq. (19). Once the scattered field coefficients are determined, the series expansion of Eq. (13) can be used to determine the scattered field acoustic pressure anywhere external to the spheroid. The total acoustic pressure is equal to the sum of the scattered and incident fields.

## III. NEAR-FIELD CALCULATIONS FOR THE PROLATE SPHEROID

Computer programs were written incorporating the theoretical development described in Sec. II. and systematic calculations investigating the effects of spheroid size, axis ratio, and the orientation and character of the incident field on the near-surface acoustic pressure distribution were performed. In this section, some results for the prolate spheroid geometry are presented. For plane wave incidence, the plane wave is assumed to propagate parallel to the *x*-*z* plane with an angle of incidence ($\theta_{\text{dir}}$) measured relative to the *y*-*z* plane, as shown in Fig. 1. The corresponding expression for the incident acoustic pressure is thus

$$p^{(i)}(\mathbf{r}) = \exp[ih(x \sin\theta_{\text{dir}} + z \cos\theta_{\text{dir}})], \tag{20}$$

where, in this case, all acoustic pressures have been nondimensionalized relative to the amplitude of the incident plane wave. The expansion coefficients for a plane wave of the form given in Eq. (20) can, in fact, be determined analytically and, according to Eq. (5.3.3) in Ref. 15,

$$A_{lm} = i^l \frac{(2-\delta_{0m})}{N_{lm}} S_{lm}(h, \cos\theta_{\text{dir}}). \tag{21}$$

For plane wave incidence, the $A_{lm}$ coefficients calculated using the numerical integration procedure of Eq. (15) were found (for both prolate and oblate geometries) to agree with the expected analytical values given in Eq. (21). For example, using ordinary trapezoidal rule numerical integration with an integration grid consisting of $4L$ steps in the $\eta$ direction and $8M$ steps in the $\phi$ direction, the numerically calculated $A_{lm}$ coefficients were typically found to agree with the theoretically predicted values given in Eq. (21) to better than one part in one million.

Figure 2 shows a surface grid plot of the calculated acoustic pressure in the *x*-*z* plane for a 45° angle of incidence plane wave incident upon a 2:1 axis ratio prolate spheroid with a spheroidal size parameter ($h$) of 10. The magnitude of the complex acoustic pressure is plotted using a 101 by 101 square grid extending from $-2$ to $+2$ in the $x$ and $z$ axis directions. (For the surface grid plots, the value of the acoustic pressure inside the spheroid is artificially set to a uniform value of 1.0.) Figure 3 provides a gray level visualization of the same data presented in the surface grid plot of Fig. 2. (For the gray level visualizations, the interior of the spheroid has been set to a uniform light gray). For the 2:1 axis ratio, $h=10$ prolate spheroid, solution convergence was obtained by using series limits of $M=12$ and $L=23$.

As can be observed in Figs. 2 and 3, the reflection of the incident plane wave from the lower surface (''incident side'') of the spheroid interferes with the oncoming incident plane wave to create a series of strong constructive and destructive interference bands. Near the upper surface (''shadow side'') of the spheroid there is a definite shielding effect except for a band of relatively high acoustic pressure that extends from the upper-right-hand surface in an outward direction that is approximately parallel with the propagation direction of the incident plane wave.

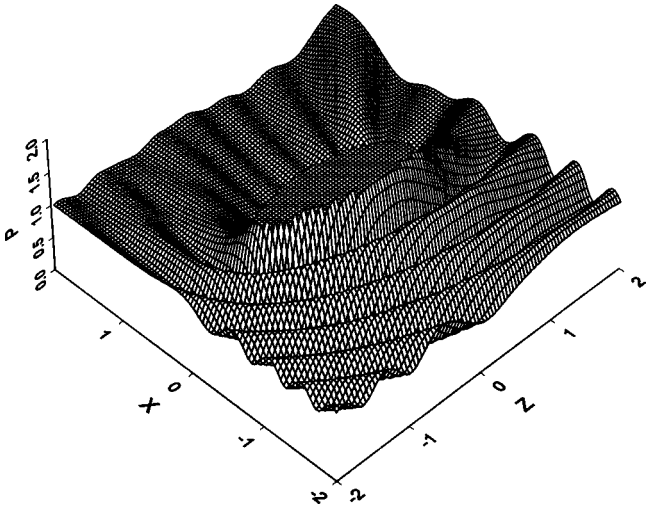


FIG. 2. A surface grid plot of the acoustic pressure in the *x*-*z* plane for a plane wave incident upon a 2:1 axis ratio prolate spheroid. Spheroid size parameter, $h=10$. Plane wave angle of incidence relative to the *y*-*z* plane, $\theta_{\text{dir}}=45°$.

By using the numerical integration procedure of Eq. (15), solutions can be obtained, not only for plane wave incidence, but for any known incident field. To demonstrate, a calculation was performed, for the same 2:1 axis ratio, $h=10$ prolate spheroid considered in Figs. 2 and 3, but now, in addition to the 45° angle of incidence plane wave, a spherical point source and a cylindrical line source (of the same frequency as the incident plane wave) are added. The spherical point source, located at $(x,y,z)=(2,0,2)$, was as-

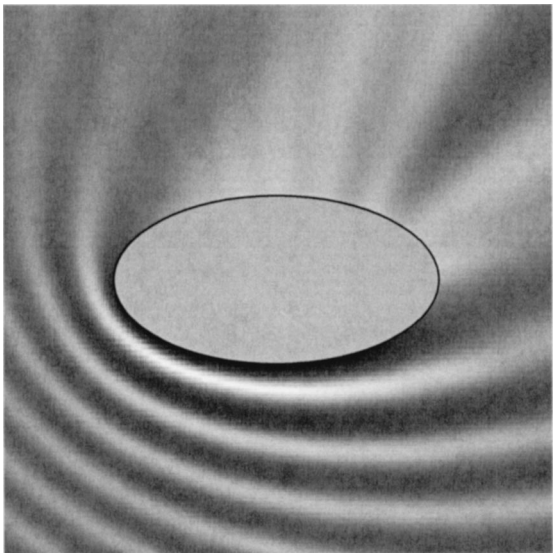

FIG. 3. Gray level visualization (white⇒low,black⇒high) of the acoustic pressure in the *x*-*z* plane for a plane wave incident upon a 2:1 axis ratio prolate spheroid. $h=10$ and $\theta_{\text{dir}}=45°$. The $z$ axis (horizontal) extends from $-2.0$ on the left to $+2.0$ on the right. The $x$ axis (vertical) extends from $-2.0$ at the bottom to $+2.0$ at the top. Maximum acoustic pressure, $p_{\max}=1.919$, and minimum acoustic pressure, $p_{\min}=0.360$.

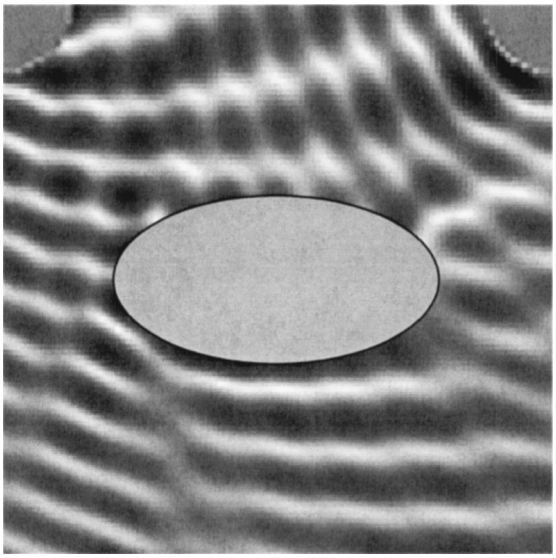

FIG. 4. Gray level visualization of the acoustic pressure in the *x*-*z* plane for a 2:1 axis ratio, $h=10$, prolate spheroid with a combined plane wave, spherical wave, and cylindrical wave sources. Plane wave: $p_{\mathrm{pl}}=1.0$, $\theta_{\mathrm{dir}}=45°$. Spherical wave: $p_{\mathrm{sph}}=0.5$, origin at (2,0,2). Cylindrical wave: $p_{\mathrm{cyl}}=3.0$, origin at (−2,0,2). The regions near the spherical and cylindrical sources have been blocked out. $p_{\max}=2.570$ and $p_{\min}=0.0199$.

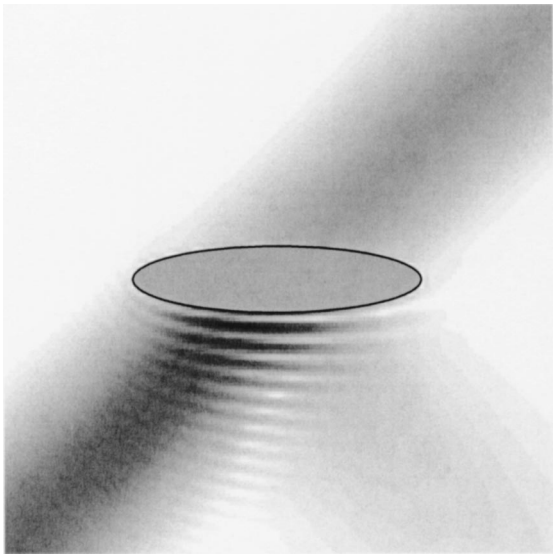

FIG. 5. Gray level visualization of the acoustic pressure in the *x*-*z* plane for a focused acoustic beam incident upon a 5:1 axis ratio prolate spheroid. $h=30$. Focused beam angle of incidence relative to the *y*-*z* plane, $\theta_{\mathrm{dir}}=45°$. Beam focused at the center of the spheroid ($x_0=0, y_0=0, z_0=0$) with a beam waist radius of $w_0=0.50$. $p_{\max}=1.939$ and $p_{\min}=0.000\,026$.

sumed to have a nominal amplitude one-half that of the incident plane wave, so

$$p_{\mathrm{sph}}(r')=(0.50/r')\exp(ihr'), \tag{22}$$

where $r'$ is the radial distance from the point source. The cylindrical line source, located at $(x,y,z)=(-2,0,2)$ and extending in the *y*-axis direction, was assumed to have a nominal amplitude three times that of the incident plane wave, so that

$$p_{\mathrm{cyl}}(r'')=3.0[J_0(hr'')+iN_0(hr'')], \tag{23}$$

where $J_0$ and $N_0$ are, respectively, the zeroth-order cylindrical Bessel functions of the first and second kinds, and $r''$ is the plane radial distance from the line source. The complex pressure field resulting from all three sources (plane wave, spherical wave, and cylindrical wave) acting simultaneously was found to be identical to the sum of the complex pressure fields from the three sources acting individually, as expected from superposition.

Figure 4 provides a gray level visualization of the near-surface acoustic pressure for the combined plane wave, spherical wave, and cylindrical wave sources. (The regions immediately adjacent to the point and line sources have been intentionally blocked out so as to omit the very high acoustic pressures that occur near these source origins.) As can be observed in Fig. 4, the combined effects of the three sources interacting with the prolate spheroid produces a finer structured interference pattern in comparison with the plane wave only case given in Fig. 3.

The solution procedure is applicable for any known incident field (e.g., focused acoustic beam, acoustic scattering from an adjacent object, etc.). A gray level visualization of the acoustic pressure distribution for the arrangement of a focused acoustic beam incident upon a 5:1 axis ratio, $h=30$ spheroidal size parameter, prolate spheroid is provided in Fig. 5. The focused beam has a nondimensionalized beam waist radius ($w_0$) of 0.50, an angle of incidence of 45°, and is focused at the center of the spheroid, $(x_0,y_0,z_0)=(0,0,0)$. The analytical equations used to evaluate the pressure distribution of the Gaussian-profiled focused acoustic beam are given in the Appendix. These equations were derived using a procedure similar to that previously applied for the development of a fifth-order corrected electromagnetic focused Gaussian beam model.[22] For the 5:1 axis ratio, $h=30$ prolate spheroid, solution convergence was obtained by using series limits of $M=26$ and $L=51$.

As can be observed in Fig. 5, the incident acoustic beam strikes the lower surface (incident side) of the prolate spheroid and the weak reflected part of the beam interferes with the oncoming incident beam to create lines of constructive and destructive interference along the lower surface of the spheroid. Since the beam waist diameter ($2w=1.0$) is bigger than the minor axis diameter of the spheroid ($2b=0.408$), much of the incident acoustic beam is not reflected but instead finds its way around the spheroid and an intact, but decreased, amplitude, acoustic beam propagates away from the shadow side of the spheroid with the same direction of propagation as that of the incident beam.

Figure 6 is for the same conditions as Fig. 5, but now the focal point of the incident beam has been moved to the left tip of the spheroid, $(x_0,y_0,z_0)=(0,0,-1.0206)$. Figure 7 is similar, but the angle of incidence is changed to 0° (i.e., end-on incidence) and the focal point moved to the top edge of the spheroid, $(x_0,y_0,z_0)=(0.2041,0,0)$.

## IV. NEAR-FIELD CALCULATIONS FOR THE OBLATE SPHEROID

In this section, some results for the oblate spheroid geometry are presented. The conditions of Figs. 8–13 corre-

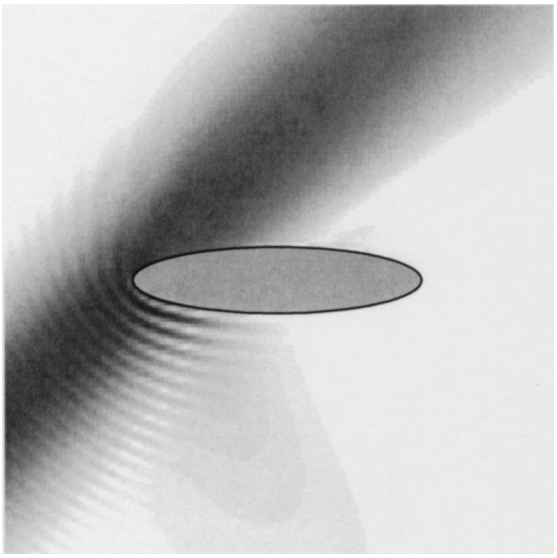

FIG. 6. Gray level visualization of the acoustic pressure in the *x*-*z* plane for a focused acoustic beam incident upon a 5:1 axis ratio prolate spheroid. $h=30$. A focused beam angle of incidence relative to the *y*-*z* plane, $\theta_{\mathrm{dir}}=45°$. The beam focused at the left tip of the spheroid ($x_0=0, y_0=0, z_0=-1.0206$) with a beam waist radius of $w_0=0.50$. $p_{\max}=1.711$ and $p_{\min}=0.000\,41$.

spond, respectively, with the conditions of Figs. 2–7, except now the spheroid is oblate, instead of prolate.

Figure 8 shows a surface grid plot of the calculated acoustic pressure in the *x*-*z* plane for a 45° angle of incidence plane wave incident upon a 2:1 axis ratio oblate spheroid with a spheroidal size parameter ($h$) of 10. Figure 9 provides a gray level visualization of the same data presented in the surface grid plot of Fig. 8. For the 2:1 axis ratio, $h=10$ oblate spheroid, solution convergence was obtained by using series limits of $M=15$ and $L=29$. As can be observed in

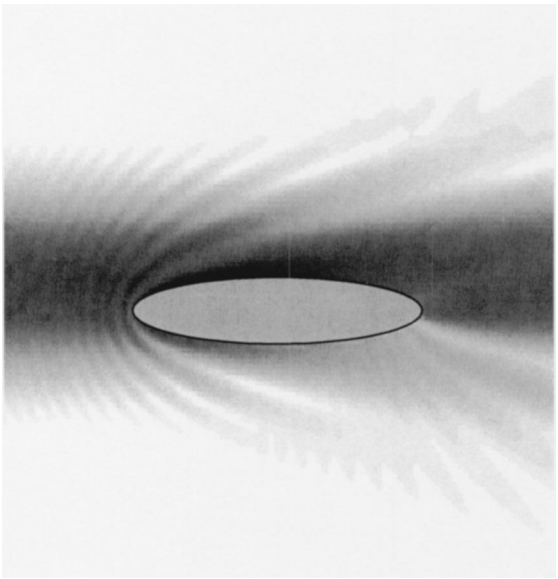

FIG. 7. Gray level visualization of the acoustic pressure in the *x*-*z* plane for a focused acoustic beam incident upon a 5:1 axis ratio prolate spheroid. $h=30$. Focused beam angle of incidence relative to the *y*-*z* plane, $\theta_{\mathrm{dir}}=0°$. The beam focused at the top edge of the spheroid ($x_0=0.2041, y_0=0, z_0=0$) with a beam waist radius of $w_0=0.50$. $p_{\max}=1.352$ and $p_{\min}=0.000\,50$.

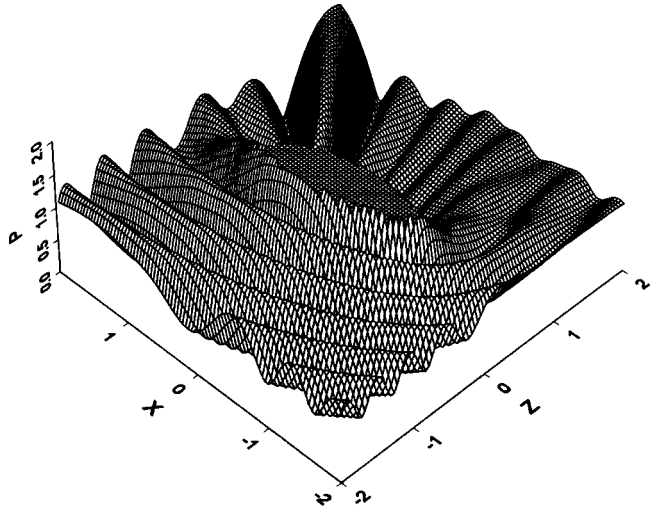


FIG. 8. Surface grid plot of the acoustic pressure in the *x*-*z* plane for a plane wave incident upon a 2:1 axis ratio oblate spheroid. $h=10$ and $\theta_{\mathrm{dir}}=45°$.

Figs. 8 and 9, the reflection of the incident plane wave from the left-hand surface (''incident side'') of the spheroid interferes with the oncoming incident plane wave to create a series of strong constructive and destructive interference bands. Near the right-hand surface (''shadow side'') of the spheroid there is some shielding and a band of relatively high acoustic pressure that extends from the upper-right-hand surface in an outward direction that is approximately parallel with the propagation direction of the incident plane wave.

Figure 10 provides a gray level visualization of the near-surface acoustic pressure for the combined plane wave, spherical wave, and cylindrical wave sources. Once again, as was observed for the prolate spheroid case, the combined effects of the three sources interacting with the oblate spheroid produces a finer structured interference pattern in comparison with the plane wave only case given in Fig. 9.

Figure 11 is for the same 5:1 axis ratio, $h=30$, on-center focused beam conditions as used in Fig. 5, but now an ob-

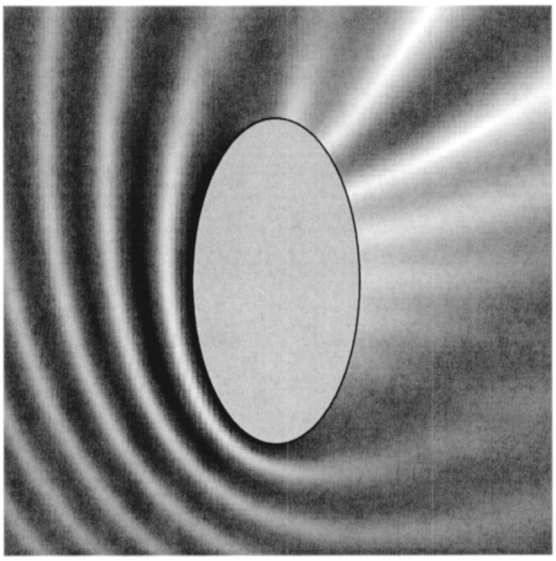

FIG. 9. Gray level visualization of the acoustic pressure in the *x*-*z* plane for a plane wave incident upon a 2:1 axis ratio oblate spheroid. $h=10$ and $\theta_{\mathrm{dir}}=45°$. $p_{\max}=1.981$ and $p_{\min}=0.0150$.

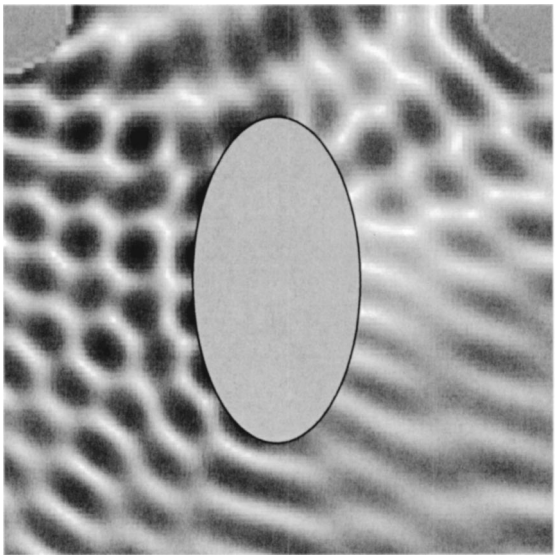

FIG. 10. Gray level visualization of the acoustic pressure in the *x*-*z* plane for a 2:1 axis ratio, $h=10$, oblate spheroid with combined plane wave, spherical wave, and cylindrical wave sources. Plane wave: $p_{\mathrm{pl}}=1.0$, $\theta_{\mathrm{dir}}=45°$. Spherical wave: $p_{\mathrm{sph}}=0.5$, origin at (2,0,2). Cylindrical wave: $p_{\mathrm{cyl}}=3.0$, origin at $(-2,0,2)$. The regions near the spherical and cylindrical sources have been blocked out. $p_{\max}=2.884$ and $p_{\min}=0.0070$.

late, instead of a prolate, spheroid is considered. For the 5:1 axis ratio, $h=30$ oblate spheroid, solution convergence was obtained by using series limits of $M=34$ and $L=55$. In the case of the oblate spheroid, since the beam waist diameter ($2w=1.0$) is smaller than the major axis diameter ($2a=2.041$), very little of the incident beam finds its way around the spheroid and almost all of the incident beam is reflected from the left-hand (incident-side) surface of the spheroid.

Figure 12 is for the same conditions as Fig. 11, but now the focal point of the incident beam has been moved to the bottom edge of the spheroid, $(x_0,y_0,z_0)=(-1.0206,0,0)$. Figure 13 is similar, but now the angle of incidence is changed to 90° (i.e., edge-on incidence) and the focal point moved to the right edge of the spheroid, $(x_0,y_0,z_0)=(0,0,0.2041)$.

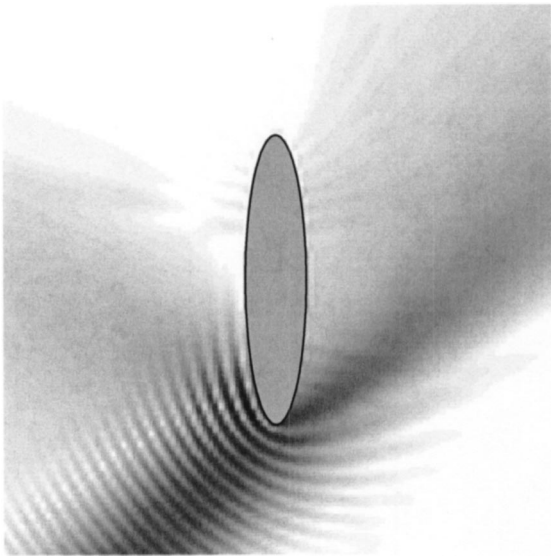

FIG. 12. Gray level visualization of the acoustic pressure in the *x*-*z* plane for a focused acoustic beam incident upon a 5:1 axis ratio oblate spheroid. $h=30$. A focused beam angle of incidence relative to the *y*-*z* plane, $\theta_{\mathrm{dir}}=45°$. The beam focused at the bottom edge of the spheroid ($x_0=-1.0206,y_0=0,z_0=0$) with a beam waist radius of $w_0=0.50$. $p_{\max}=1.935$ and $p_{\min}=0.0024$.

## V. CONCLUSIONS

A general spheroidal coordinate separation-of-variables solution has been developed for the determination of the

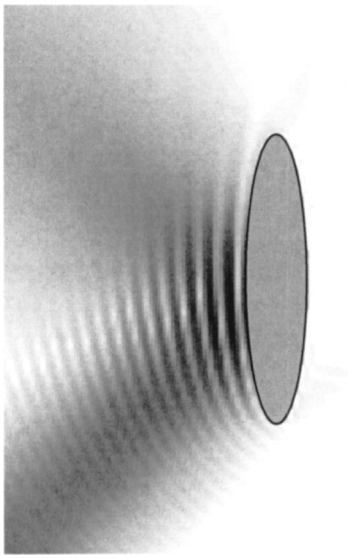

FIG. 11. Gray level visualization of the acoustic pressure in the *x*-*z* plane for a focused acoustic beam incident upon a 5:1 axis ratio oblate spheroid. $h=30$. The focused beam angle of incidence relative to the *y*-*z* plane, $\theta_{\mathrm{dir}}=45°$. The beam focused at the center of the spheroid ($x_0=0,y_0=0,z_0=0$) with a beam waist radius of $w_0=0.50$. $p_{\max}=1.999$ and $p_{\min}=0.000\,50$.

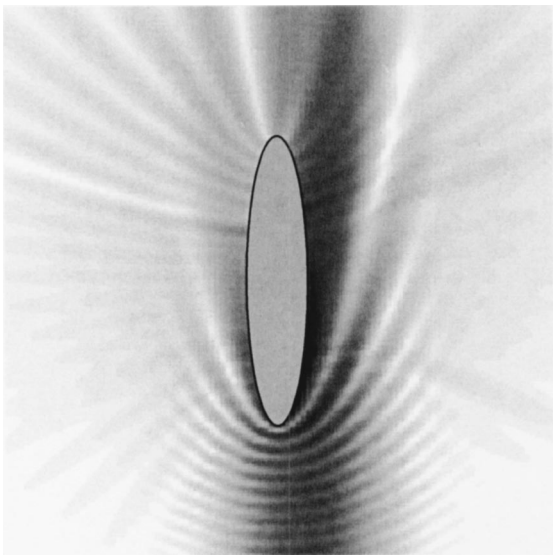

FIG. 13. Gray level visualization of the acoustic pressure in the *x*-*z* plane for a focused acoustic beam incident upon a 5:1 axis ratio oblate spheroid. $h=30$. Focused beam angle of incidence relative to the *y*-*z* plane, $\theta_{\mathrm{dir}}=90°$. The beam focused at the right edge of the spheroid ($x_0=0,y_0=0,z_0=0.2041$) with a beam waist radius of $w_0=0.50$. $p_{\max}=1.668$ and $p_{\min}=0.0061$.

acoustic pressure distribution near the surface of a rigid spheroid for a monofrequency incident acoustic field of arbitrary character. Calculated results have been presented, for both the prolate and oblate geometries, demonstrating the manner in which the orientation and character of the incident field can affect the subsequent near-surface acoustic pressure distribution. As an example of one possible application, a comparison of the near-field acoustic pressure distribution with the corresponding farfield scattering could be used to assist in developing insight into the physical origins of the angle-dependent structure exhibited in the farfield scattering pattern.

In general, higher axis ratio and/or higher size parameter objects require a larger number of series terms for convergence. The software programs used for the calculations presented here have an inherent upper spheroidal function limit of $M=40$ and $L=80$. With this limitation, calculations have been successfully performed for axis ratios up to 10:1 and spheroidal size parameters ($h$) up to 40.

## APPENDIX: FOCUSED ACOUSTIC BEAM MODEL

A fifth-order corrected model for the acoustic pressure of a focused Gaussian-profiled beam with a beam waist radius of $w_0$ propagating in the $+z$-axis direction is as follows. An $\exp(-i\omega t)$ time dependence is assumed:

$$p(x,y,z)=p_r\left(1+s^2\frac{\psi_2}{\psi_0}+s^4\frac{\psi_4}{\psi_2}\right)iQ \times\exp(-i\rho^2Q)\exp(i\zeta/s^2), \tag{A1}$$

where

$$s=1/(hw_0),\quad \rho^2=(x^2+y^2),\quad \zeta=z/(hw_0),\quad Q=1/(i-2\zeta), \tag{A2}$$

and

$$\frac{\psi_2}{\psi_0}=(+2iQ+i\rho^4Q^3)$$

and

$$\frac{\psi_4}{\psi_2}=(-6Q^2-3\rho^4Q^4-2i\rho^6Q^5-\rho^8Q^6/2). \tag{A3}$$


[1] R. D. Spence and S. Granger, "The scattering of sound from a prolate spheroid," J. Acoust. Soc. Am. **23**, 701–706 (1951).

[2] A. Silbiger, "Scattering of sound by an elastic prolate spheroid," J. Acoust. Soc. Am. **35**, 564–570 (1963).

[3] T. B. A. Senior, "The scattering from acoustically hard and soft prolate spheroids for axial incidence," Can. J. Phys. **44**, 655–667 (1966).

[4] G. Lauchle, "Short-wavelength acoustic diffraction by prolate spheroids," J. Acoust. Soc. Am. **58**, 568–575 (1975).

[5] G. Lauchle, "Short-wavelength backscattering by a prolate spheroid," J. Acoust. Soc. Am. **58**, 576–580 (1975).

[6] W. K. Blake and G. A. Wilson, "Short-wavelength diffracted surface pressures on a rigid prolate spheroid," J. Acoust. Soc. Am. **61**, 1419–1426 (1977).

[7] A. Germon and G. C. Lauchle, "Axisymmetric scattering of spherical waves by a prolate spheroid," J. Acoust. Soc. Am. **65**, 1322–1327 (1979).

[8] R. H. Hackman, G. S. Sammelmann, K. L. Williams, and D. H. Trivett, "A reanalysis of the acoustic scattering from elastic spheroids," J. Acoust. Soc. Am. **83**, 1255–1266 (1988).

[9] G. S. Sammelmann, D. H. Trivett, and R. H. Hackman, "High-frequency scattering from rigid prolate spheroids," J. Acoust. Soc. Am. **83**, 46–54 (1988).

[10] V. K. Varadan, V. V. Varadan, L. R. Dragonette, and L. Flax, "Computation of rigid body scattering by prolate spheroids using the T-matrix approach," J. Acoust. Soc. Am. **71**, 22–25 (1982).

[11] L. Flax and L. R. Dragonette, "Analysis and computation of the acoustic scattering by an elastic prolate spheroid obtained from the T-matrix formulation," J. Acoust. Soc. Am. **71**, 1077–1082 (1982).

[12] G. C. Gaunaurd and M. F. Werby, "Interpretation of the three-dimensional sound fields scattered by submerged elastic shells and rigid spheroidal bodies," J. Acoust. Soc. Am. **84**, 673–680 (1988).

[13] Z. Ye, E. Hoskinson, R. K. Dewey, L. Ding, and D. M. Farmer, "A method for acoustic scattering by slender bodies. I. Theory and verification," J. Acoust. Soc. Am. **102**, 1964–1976 (1997).

[14] A. Maciulaitis, J. M. Seiner, and T. D. Norum, "Sound scattering by rigid oblate spheroids, with implication to pressure gradient microphones," NASA, 1976, TN D-8140, pp. 1–40.

[15] C. Flammer, *Spheroidal Wave Functions* (Stanford University Press, Stanford, CA, 1957).

[16] J. P. Barton, "Internal and near-surface electromagnetic fields for a spheroidal particle with arbitrary illumination," Appl. Opt. **34**, 5542–5551 (1995).

[17] P. M. Morse and H. Feshbach, *Methods of Theoretical Physics* (McGraw-Hill, New York, 1953).

[18] J. A. Stratton, P. M. Morse, L. J. Chu, J. D. C. Little, and F. J. Corbato, *Spheroidal Wave Functions* (Wiley, New York, 1956).

[19] J. J. Bowman, T. B. A. Senior, and P. L. E. Uslenghi, *Electromagnetic and Acoustic Scattering by Simple Shapes* (North-Holland, Amsterdam, 1969).

[20] M. Abramowitz and I. A. Stegun, *Handbook of Mathematical Functions With Formulas, Graphs, and Mathematical Tables* (Dover, New York, 1970).

[21] S-J Zhang and J. Jin, *Computation of Special Functions* (Wiley, New York, 1996).

[22] J. P. Barton and D. R. Alexander, "Fifth-order corrected electromagnetic field components for a fundamental Gaussian beam," J. Appl. Phys. **66**, 2800–2802 (1989).